



Carbon/iron co-product from clean hydrogen production as a tri-functional adsorbent and catalyst for efficient wastewater treatment

Yuan Yuan Yao, Yuqi Pan, Leo Lai, Zixun Yu, Jiayang Chen, Yanxi Yu, Terrence Darma, Yongwen Tao, Liuyue Cao, Benjamin Chivers, Xia Zhong, Li Wei^{*}, Yuan Chen^{*}

The University of Sydney, School of Chemical and Biomolecular Engineering, Darlington, NSW 2006, Australia

ARTICLE INFO

Keywords:

Sustainable hydrogen production
Carbon adsorbent
Hydrogen peroxide synthesis
Heterogeneous Fenton catalyst
Recyclable catalyst

ABSTRACT

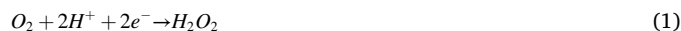
Clean hydrogen production via methane pyrolysis ($\text{CH}_4 \rightarrow 2\text{H}_2 + \text{C}$) generates large quantities of solid carbon. Realizing their applications is a critical gap to enable its broader adoption. Here, we show that carbon nano onions encapsulated with iron cores ($\text{Fe}@\text{CNO}$) produced in CH_4 pyrolysis using low-cost Fe ore catalysts can serve as a tri-functional adsorbent and catalyst for organic contaminant degradation. $\text{Fe}@\text{CNO}$ has a high adsorption capacity and fast pseudo-second-order adsorption kinetics for antibiotics in wastewater. Surface oxidized $\text{Fe}@\text{CNO}$ presents a high catalytic activity for in situ hydrogen peroxide production. $\text{Fe}@\text{CNO}$ is also an efficient heterogeneous Fenton catalyst to degrade adsorbed antibiotics. Further, the Fe core is magnetic, enabling easy separation from solvents as reusable adsorbents and catalysts. We demonstrate that the adsorption and electro-Fenton process applies to various organic pollutants in different water matrices. This opens a new strategy for utilizing co-products from H_2 production for sustainable environmental applications.

1. Introduction

Hydrogen (H_2) is a critical industrial feedstock, and it can also decarbonize various economic sectors to realize a sustainable H_2 economy. However, 95% of current H_2 production comes from fossil fuels. Methane (CH_4) is the second most significant contributor to climate change [1]. CH_4 pyrolysis, in which CH_4 is split into H_2 and solid carbon without releasing CO_2 , is a promising cost-effective alternative for H_2 production. Its cost-effectiveness is heavily dependent on the usage of solid carbon because the H_2 to solid carbon mass ratio is 1/3 in its products [2]. Recent techno-economic analysis and carbon footprint assessment of CH_4 pyrolysis indicate that the price of H_2 could be minimal if carbon co-products can be sold [3–5]. However, solid carbon from CH_4 pyrolysis using various catalysts often contains impurities that must be removed for many applications [6–9], adding appreciable costs. Finding large-scale applications for solid carbon from CH_4 pyrolysis without expensive purification is a potential solution to addressing the challenge.

Toxic organic contaminants in wastewater released from pesticides, dyes, antibiotics, and personal care products are an increasing environmental problem [10,11]. Conventional wastewater treatment processes cannot effectively degrade these contaminants. Advanced

oxidation processes generate strong reactive oxygen species (ROSs) that can effectively degrade them [12–18]. The homogenous Fenton process is one of the most widely used advanced oxidation processes, in which hydrogen peroxide (H_2O_2) and a Fenton reagent (e.g., ferrous ions (Fe^{2+})) are added to the wastewater at the pH of around 3 to generate ROSs (Eq. 2) [19,20]. However, the homogenous Fenton process has significant drawbacks. It also produces large amounts of Fe sludge (i.e., $\text{Fe}(\text{OH})_3$) as secondary wastes, and handling explosive high-concentration H_2O_2 also has high cost and safety risks. An alternative is electro-Fenton processes, in which H_2O_2 is synthesized in situ by an oxygen reduction reaction (ORR, Eq. 1) [19–27]. There are two types of electro-Fenton processes: homogenous and heterogeneous. In homogenous electro-Fenton processes, a Fenton reagent (e.g., Fe^{2+}) still needs to be added in a narrow pH range, e.g., 2.8–3.5, resulting in Fe sludge formation. In heterogeneous electro-Fenton processes, Fe sludge formation is significantly reduced by anchoring Fe species in heterogeneous Fe catalysts that minimize free Fe^{2+} leaching and promote $\text{Fe}^{3+}/\text{Fe}^{2+}$ regeneration via direct reduction on electrodes (Eq. (3)) [28]. Heterogeneous processes can also work under broader pH conditions than homogenous Fenton processes [26,29–36].



^{*} Corresponding authors.

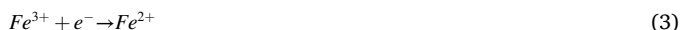
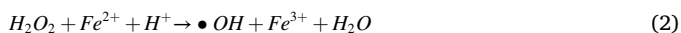
E-mail addresses: l.wei@sydney.edu.au (L. Wei), yuan.chen@sydney.edu.au (Y. Chen).

<https://doi.org/10.1016/j.apcatb.2023.123380>

Received 2 July 2023; Received in revised form 27 September 2023; Accepted 7 October 2023

Available online 17 October 2023

0926-3373/© 2023 The Author(s). Published by Elsevier B.V. This is an open access article under the CC BY-NC-ND license (<http://creativecommons.org/licenses/by-nc-nd/4.0/>).



However, heterogeneous electro-Fenton processes have several limitations. First, although various heterogeneous Fe catalysts have been explored [37–39], their reaction rate is usually slower than homogeneous processes in which Fe^{2+} is directly added. Further, most heterogeneous Fe catalysts cannot be recovered and reused for multiple reaction cycles. Second, although low-cost carbon materials and composites are active ORR catalysts for H_2O_2 synthesis [37,38,40–47], the H_2O_2 production rate is often low, limited by low O_2 solubility in water and slow mass transfer rate to reach active catalytic sites [48–52]. Third, the concentration of organic contaminants in typical wastewater is often not high. For example, the concentration of antibiotics in municipal water is much less than 10 mg/L [53], but the volume of municipal water is extra large. Treating large volumes of wastewater with low organic contaminant concentrations is not economical. Although some studies have coupled an adsorption process to concentrate organic contaminants in wastewater that enable more efficient advanced oxidation processes [54], the high cost and lack of reusability of adsorbents significantly increase operational costs.

Here, we demonstrate that Fe particles encapsulated by carbon nano onions (Fe@CNO), a co-product of clean H_2 production via CH_4 pyrolysis using low-cost Fe ore catalysts, can serve as a tri-functional adsorbent and catalyst for the efficient degradation of organic contaminants in wastewater treatment. Fig. 1 provides a schematic illustration of a new wastewater treatment process with four steps. (1) Low-concentration organic contaminants in wastewater are first enriched on Fe@CNO by adsorption. (2) Fe@CNO saturated with organic contaminants is separated from the wastewater using an external magnetic field to achieve solid/liquid separation. (3) In an electro-Fenton process, H_2O_2 is in situ synthesized on the cathode made of oxidized Fe@CNO in a two-electrode electrolyzer with a neutral electrolyte (0.05 M Na_2SO_4) using electricity and air. Simultaneously, Fe@CNO saturated with organic contaminants is added to the electrolyte, which serves as a

heterogeneous Fenton catalyst to degrade adsorbed organic contaminants and regenerate Fe@CNO. (4) Regenerated Fe@CNO is separated from the electrolyte by the external magnetic field to achieve solid/liquid separation so they can be reused in the next cycle of the adsorption step. Fe@CNO plays three roles in this wastewater treatment process: an adsorbent for organic contaminants, an electrocatalyst for H_2O_2 synthesis, and a heterogeneous Fenton catalyst for the electro-Fenton reaction. We first discuss the properties and performance of Fe@CNO for each of the three roles and then demonstrate the feasibility and cost-effectiveness of the entire process for efficient wastewater treatment.

2. Materials and methods

2.1. Synthesis of Fe@CNO

Fe@CNO were synthesized by catalytic methane pyrolysis using a Limonite Fe ore from Western Australia as catalysts. The iron ore comprises 88.00 wt% Fe_2O_3 , 3.34 wt% SiO_2 , and 1.16 wt% Al_2O_3 . CH_4 (5.5 m^3/h , standard conditions, at an hourly gas space velocity of 12.22 $\text{L}/\text{g}_{\text{cat}}$) flowed through a distributor plate from the bottom of a 2-inch diameter fluidized bed reactor at 890 °C and 6 bar. 150 g of Fe ore particles of 100–200 μm in size were injected into the reactor from the top every 20 min over 6 h. CH_4 interacted with Fe ore particles, and they would disintegrate into nanometer-scale fragments. CH_4 then decomposed into H_2 and graphitic carbon layers on Fe surfaces. Fe ore particles' mass density decreased with the growth of carbon materials and subsequently were carried out in the reactor by the upward gas stream containing H_2 and unreacted CH_4 . Solid materials were separated by a sintered metal plate, yielding Fe@CNO. More synthesis details are available in our previous study [55]. We also synthesized Fe@CNO using high-purity Fe_2O_3 (>99.9 wt%) micrometer-size particles under similar reaction conditions to investigate the potential effect of impurities in Fe ores.

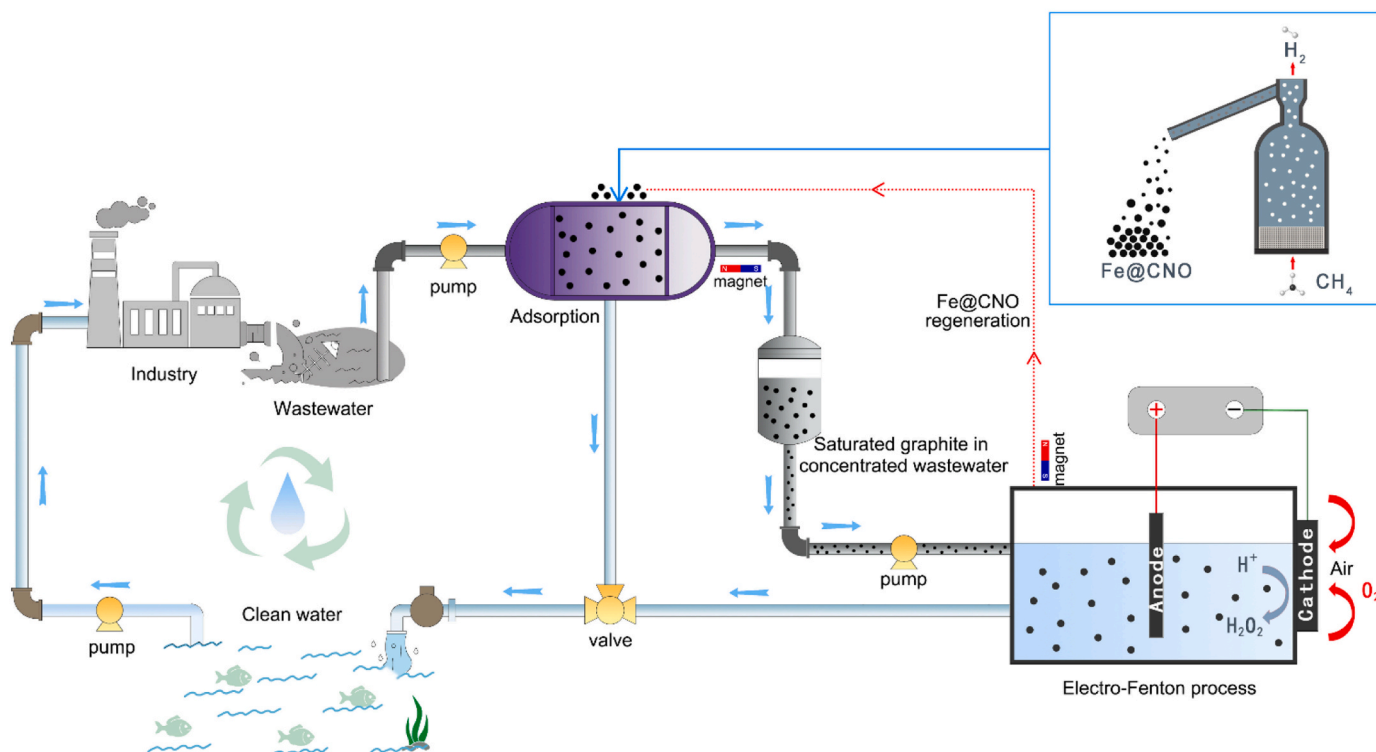


Fig. 1. Schematic illustration of Fe@CNO-enabled wastewater treatment process.

2.2. Oxidation of Fe@CNO

Fe@CNO (1 g) was mixed with nitric acid (HNO₃, 12 M, 200 mL) and refluxed at 90 °C for different periods of 1, 3, or 6 h to introduce oxygen functional groups on carbon surfaces. The slurries obtained after oxidation were centrifuged and washed with water and ethanol several times until their pH reached 7. Then, they were dried at 60 °C in a vacuum oven overnight.

2.3. Material characterization

The morphology of Fe@CNO was first examined by scanning electron microscopy (SEM, Zeiss, Gemini Ultra Plus). Their atomic structures were characterized by transmission electron microscopy (TEM, JEOL, JEM-2100F). The thermogravimetric analysis (TGA) of Fe@CNO was performed using a TG analyzer (TA Instruments, Q500) under airflow from 30° to 800°C at the heating rate of 10 °C/min. Their X-ray diffraction (XRD) patterns were recorded using a diffractometer (PANalytical X'Pert PRO) under Cu-Kα radiation. Raman spectra were collected using a Raman spectrometer (Renishaw, inVia Reflex) under a 532 nm excitation laser. The specific surface area of Fe@CNO was measured by N₂ physisorption using a gas adsorption analyzer (Quantumchrome, Autosorb iQ). Their pore size distributions were estimated using the quenched solid-state BJH model. Their surface chemical compositions were analyzed by X-ray photoelectron spectroscopy (XPS, Thermo, K-Alpha+) equipped with an Al Kα X-ray source (1486.6 eV). The elemental composition of iron ore catalysts and ashes obtained after TGA was also analyzed by X-ray fluorescence spectroscopy (XRF, Panalytical, PW2400 WDXRF) and inductively coupled plasma optical emission spectroscopy (ICP-OES, Perkin Elmer Avio 500).

2.4. Adsorption of tetracycline on Fe@CNO

The batch adsorption experiments of tetracycline on Fe@CNO were conducted with a fixed Fe@CNO concentration of 20 mg/L. The mixture was mechanically shaken at 200 rpm and 25 °C. The initial tetracycline solution in different concentrations from 0.5 to 10 mg/L was prepared by diluting its stock solution at 200 mg/L. Next, the initial tetracycline concentration of 4 mg/L was used in kinetic experiments. Small samples were collected at different intervals (2, 10, 30 min, 1, 2, 4, 8, 21, and 24 h). Tetracycline concentration was determined by high-performance liquid chromatography equipped with an ultraviolet detector at 365 nm using methanol, acetonitrile, and 0.01 M oxalic acid as the liquid phase. The time-dependent adsorption capacity was determined by Eq. (4):

$$q_t = \frac{(C_0 - C_t)V}{m} \quad (4)$$

where q_t is the adsorption capacity (mg/g); c_0 and c_t (mg/L) are the tetracycline concentration at the initial and t moment, respectively, V (0.5 L) is the volume of solution, and m (0.010 g) is the mass of the Fe@CNO adsorbent. The isotherms obtained in adsorption experiments were evaluated using Langmuir and Freundlich models. The kinetic data were fitted with *pseudo*-first order and *pseudo*-second order equations. The details are in the text related to Table S2 in the Supporting Information.

2.5. Electrocatalytic performance of Fe@CNO-O

The electrocatalytic performance of Fe@CNO-O for H₂O₂ synthesis via ORR was first evaluated using an electrochemical workstation (CHI 760E, Chenhua Instruments) in a three-electrode configuration. 5 mg of Fe@CNO-O was dispersed in 1 mL isopropyl alcohol containing 50 μL of 5 wt% Nafion solution as catalyst ink. Then, 5 μL catalyst ink was deposited on glass carbon electrodes (5.5 mm diameter) as working electrodes. A platinum mesh was used as the counter electrode, and a saturated calomel electrode (SCE) was used as the reference electrode.

The rotating ring-disk electrode (RRDE) tests were conducted at a rotation speed of 1600 rpm. All potentials were measured against an SCE and converted to the reversible hydrogen electrode (RHE) reference by Eq. (5) below:

$$E_{(\text{vs. RHE})} = E_{(\text{vs. SCE})} + 0.240\text{V} + 0.0591\text{V} \times \text{pH} \quad (5)$$

The ring electrode potential was set at 1.2 V (vs. RHE). The following equations (Eqs. (6) and (7)) calculated the selectivity to H₂O₂ and electron transfer number (n):

$$\text{H}_2\text{O}_2 \text{ Selectivity} = 200 \times \frac{I_r/N}{I_D + I_r/N} \quad (6)$$

$$n = 4 \times \frac{I_d}{I_d + I_r/N} \quad (7)$$

where I_r is the current intensity of the ring electrode, I_d is the current intensity of the disk electrode, and N is the collection efficiency of the Pt ring electrode used at 0.37.

2.6. Electrochemical synthesis of H₂O₂

The electrochemical synthesis of H₂O₂ was carried out using a two-electrode electrolyzer with a single compartment filled with 100 mL of 0.05 M Na₂SO₄ as the electrolyte. The gas diffusion electrodes (GDEs) used as cathodes were fabricated by spraying the mixture (about 4 mL) of hydrophobic PTFE (20 wt%) and Fe@CNO-O mixture (80 wt%) on the hydrophobic side of carbon cloth substrates. Their effective catalytic area is 12 cm² with a Fe@CNO-O mass loading of 5 mg/cm. Before use, GDEs were further calcined at 300 °C in Ar for 1 h before use. The anodes were fabricated by spraying commercial IrO₂ catalysts (2 mg/cm²) mixed with PFTE at the 4:1 mass ratio on a Ti mesh (12 cm²). H₂O₂ synthesis was carried out under the constant current density of 10, 20, 30, or 40 mA/cm². The used cathodes were rinsed with ultrapure water and dried at room temperature before carrying out stability tests.

The concentration of synthesized H₂O₂ was quantified using a traditional Ce(SO₄)₂ titration method, in which a Ce⁴⁺ solution in yellow color was reduced by H₂O₂ to colorless Ce³⁺. Ce(SO₄)₂ solution (1 mM) was prepared by dissolving 33.2 mg of Ce(SO₄)₂ in 100 mL of 0.5 M H₂SO₄ solution. H₂O₂ of known concentrations was added to the Ce(SO₄)₂ solution to obtain a calibration curve. The concentration changes were measured using an absorption spectrometer (Shimadzu, UV 2550) at 316 nm. Based on the linear relationship between the signal intensity measured by the spectrometer and the Ce⁴⁺ concentration, the concentration of synthesized H₂O₂ was determined.

The current efficiency (CE) of H₂O₂ synthesis was calculated using the following equation (Eq. (8)):

$$CE = \frac{2CVF}{It} \times 100\% \quad (8)$$

where C is H₂O₂ concentration (mol/L), V is the volume of electrolyte (L), F is the Faraday constant (96,485 C/mol), I is the current density (A), and t is the reaction time (h).

The electric energy consumption (EEC, kWh/kg) of H₂O₂ synthesis was calculated by the following equation (Eq. (9)):

$$EEC = \frac{1000UIt}{CV} \quad (9)$$

where U and I are the applied voltage (V) and current (A), respectively, t is the reaction time (h), C is the concentration of synthesized H₂O₂ (mg/L), and V is the volume of electrolyte (L).

2.7. Electro-Fenton process with in situ H₂O₂ generation

The electro-Fenton process was conducted in the single-compartment two-electrode electrolyzer filled with 0.05 M Na₂SO₄ electrolyte and different quantities of tetracycline-saturated Fe@CNO.

The initial concentration of organic contaminants (tetracycline) was set at 20 or 100 mg/L according to the adsorption capacity of Fe@CNO. The electrolytes' pH was also varied from 3.0 to 10.0 using buffer solutions. During the reaction, 1 mL of electrolyte was extracted after different intervals and filtered through a PTFE membrane (0.22 μm pore size) to be analyzed by HPLC to determine the concentration of tetracycline. After 5 h of the electro-Fenton reaction, Fe@CNO in the electrolyte was separated using an external magnet for other tests and reuses. For comparison, the electrochemical oxidation was also carried out as a control experiment; 100 mg/L tetracycline was directly added for treatment using the same electrolyzer under the current density of 40 mA/cm² without adding Fe@CNO.

For realistic wastewater tests, 100 mg/L of tetracycline adsorbed on Fe@CNO was added to natural water from a pond at Victoria Park in Sydney (with a total organic content (TOC) of 30 mg/L). HPLC then quantified the concentration of tetracycline during the electro-Fenton reaction. The TOC of extracted samples was also measured using a TOC analyzer (Shimadzu, TOC-L) by catalytic oxidation on Pt catalysts at 680 °C. The TOC analyzer was calibrated by potassium phthalate (Sigma, 99.9%).

The energy consumption per unit of TOC (EC_{TOC} , kWh g TOC⁻¹) was calculated using the following Eq. (10):

$$EC_{\text{TOC}} = \frac{UIt}{\Delta\text{TOC} \times V} \quad (10)$$

Mineralization current efficiency (MCE) was calculated by Eq. (11) [56]:

$$MCE = \frac{nFV\Delta\text{TOC}}{4.32 \times 10^7 mIt} \times 100\% \quad (11)$$

where n is the number of electrons consumed for the complete mineralization of a pollutant molecule (i.e., $\text{C}_{22}\text{H}_{24}\text{N}_2\text{O}_8 + 42 \text{H}_2\text{O} \rightarrow 22\text{CO}_2 + 108 \text{H}^+ + 2\text{NO}_3^- + 106\text{e}^-$), F is the Faraday constant (96,487 C/mol), V is the electrolyte volume (L), ΔTOC is the experimental TOC decay (mg L⁻¹), 4.32×10^7 is a conversion factor to homogenize units ($3600 \text{ s h}^{-1} \times 12,000 \text{ mg of C mol}^{-1}$), m is the carbon atom number of

the pollutant molecule, I is the applied current (A), and t is the reaction time (h).

2.8. Reaction mechanism studies

Electron paramagnetic resonance spectroscopy EPR was carried out to identify ROS generated during the electro-Fenton process. 5,5-dimethyl-1-pyrroline-N-oxide (DMPO) and 2,2,6,6-tetramethylpiperidine (TEMP) were used as trapping agents to capture $\cdot\text{OH}$ and $^1\text{O}_2$. It was tested using a Bruker EMX X Plus-10/12 EPR with the following settings: center field of 3420 G, sweep width with 200 G, microwave frequency of 9.854 GHz, micropower of 20 mW, modulation amplitude of 1 G, and modulation frequency of 100 kHz.

3. Results and discussion

3.1. Synthesis and characterization of Fe@CNO

Fe@CNO was synthesized as a co-product of H₂ by catalytic CH₄ pyrolysis ($\text{CH}_4 \rightarrow 2\text{H}_2 + \text{C}$) on Fe ore catalysts, as described in the Experimental Section. The SEM image in Fig. 2A shows that the synthesized material has several carbon morphologies, including CNOs, carbon nanotubes, and micro carbon shells. CNOs are the dominant carbon morphology comprising concentric graphene layers radiating from a central Fe catalyst core. The TEM images in Fig. 2B show concentric graphene layers in the shell encapsulating a zero-valent Fe particle core, forming a core-shell structure. A back-scatter image superimposed on an SEM image in Fig. 2C and D shows Fe cores inside CNOs. Such a structure is beneficial to facilitate electron transfer from the Fe core to the outer particle surface and prevent the leaching of Fe.

The TGA profile of Fe@CNO in Fig. 2E indicates that the residue ash mass ratio after oxidation in air at 800 °C is 28.0 wt%. The ash comes from the oxidation of encapsulated Fe into Fe₂O₃, which counts for 19.6 wt% of Fe in Fe@CNO. The morphology of Fe@CNO was further characterized by N₂ physisorption. Fig. 2F shows a typical type III adsorption isotherm with an H3 hysteresis loop, suggesting slit-shaped

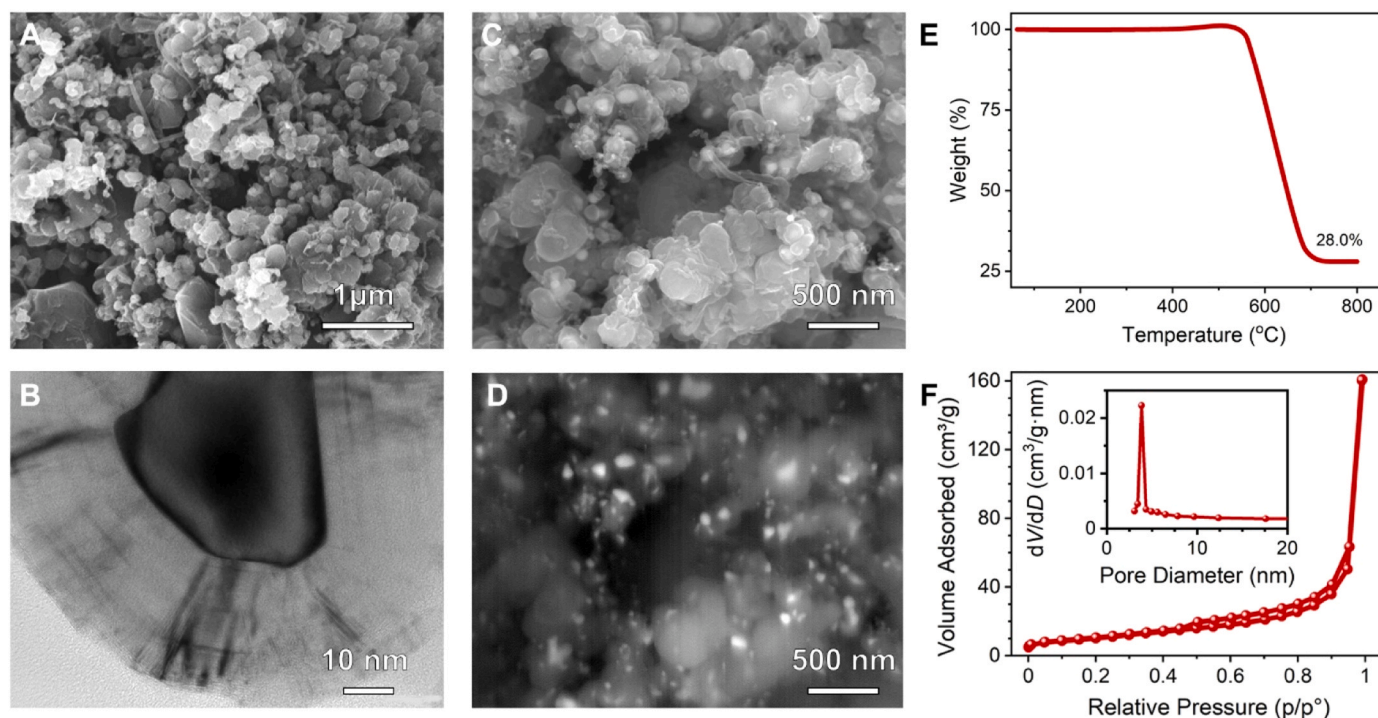


Fig. 2. Physicochemical properties of Fe@CNO, (A) An SEM image, (B) A TEM image, (C, D) an SEM image and a back-scatter image superimposed on the SEM image, (E) TGA profile of Fe@CNO, (F) N₂ physisorption isotherm of Fe@CNO and its pore size distribution (insert).

mesopores formed among Fe@CNO. Its specific surface area is 39 m²/g, with mesopores centered around 3.8 nm.

To investigate potential effects of the impurities in Fe ore catalysts on the properties of Fe@CNO, we analyzed Fe ore catalysts and the ash residues of Fe@CNO obtained after TGA by XRF. XRF results in Table S1 in the Supporting Information and the TGA results above indicate that Fe accounts for 18.7 wt% in Fe@CNO. Al is the second most abundant metal species in the Fe ore, resulting in 0.42 wt% Al residues in Fe@CNO. Alternatively, ICP-OES analysis indicated that the weight fraction of Fe in Fe@CNO is around 15.2 wt%, and Al is around 0.18 wt%. The lower weight contents from ICP-OES results can be attributed to the fact that thick graphitic layers encapsulate some Fe and Al; thus, they can not be leached out during the acid digestion when preparing ICP-OES samples. For comparison, we also carried out CH₄ pyrolysis using high-purity Fe₂O₃ particles as a catalyst. The resulting Fe@CNO was also analyzed by TGA and SEM. Fig. S1 in the Supporting Information shows that Fe accounts for 16.1 wt% in Fe@CNO, similar to that obtained using Fe ore catalysts. Further, Fe@CNO synthesized using high-purity Fe₂O₃ also has a similar morphology as those obtained using Fe ore catalysts. We conclude that the effects of the impurities in Fe ore catalysts on Fe@CNO are minimal.

3.2. Adsorption isotherms and kinetics of Fe@CNO

Tetracycline (C₂₂H₂₄N₂O₈) is a common oral antibiotic that has been found in many wastewaters. We used it as a model organic contaminant in this study. As the concentration of antibiotics in sewage is usually below 10 mg/L [53], we focused on the adsorption of tetracycline on Fe@CNO (at a fixed Fe@CNO concentration of 20 mg/L) with an initial

tetracycline concentration ranging from 0.5 to 10 mg/L. Their adsorption isotherms in Fig. 3A show that Fe@CNO's equilibrium adsorption capacity (q_e) increases with the equilibrium tetracycline concentration (c_e) by slowly decreasing slopes. When the initial tetracycline concentration is 4 mg/L, c_e concentration is 1.56 mg/L, indicating a removal efficiency higher than 60% by adsorption on Fe@CNO.

Fe@CNO saturated with tetracycline can be easily separated from the solution using an external magnet, which can be attributed to its magnetic Fe core (see the video in the Supporting Information). To confirm the magnetic property of Fe@CNO, a room temperature magnetization measurement was carried out using a vibrating sample magnetometer in an external magnetic field range between -20 kOe and +20 kOe. Fig. S2 in the Supporting Information shows that Fe@CNO is nearly superparamagnetic, and its magnetization value at the maximum applied field is 21.8 emu/g.

Supplementary material related to this article can be found online at doi:10.1016/j.apcatb.2023.123380.

Two classic adsorption models, the Langmuir and Freundlich models, were used to fit the adsorption isotherms (see details in the Experimental Section), as shown in Fig. 3B and C and listed in Table S2 in the Supporting Information. The fitting results suggest that tetracycline is adsorbed on the surface of Fe@CNO in a monolayer when the initial tetracycline concentration is low [57]. The homogeneous monolayer adsorption changes into heterogeneous multilayer adsorption with increased initial tetracycline concentration [58]. Langmuir and Freundlich's models fit experimental data well in the tested tetracycline concentration range. Based on the Langmuir model, the ideal maximum adsorption capacity (q_m) is 204.8 mg/g, similar to the experimentally measured 199.5 mg/g at the c_e of 6.01 mg/L. The adsorption isotherm in

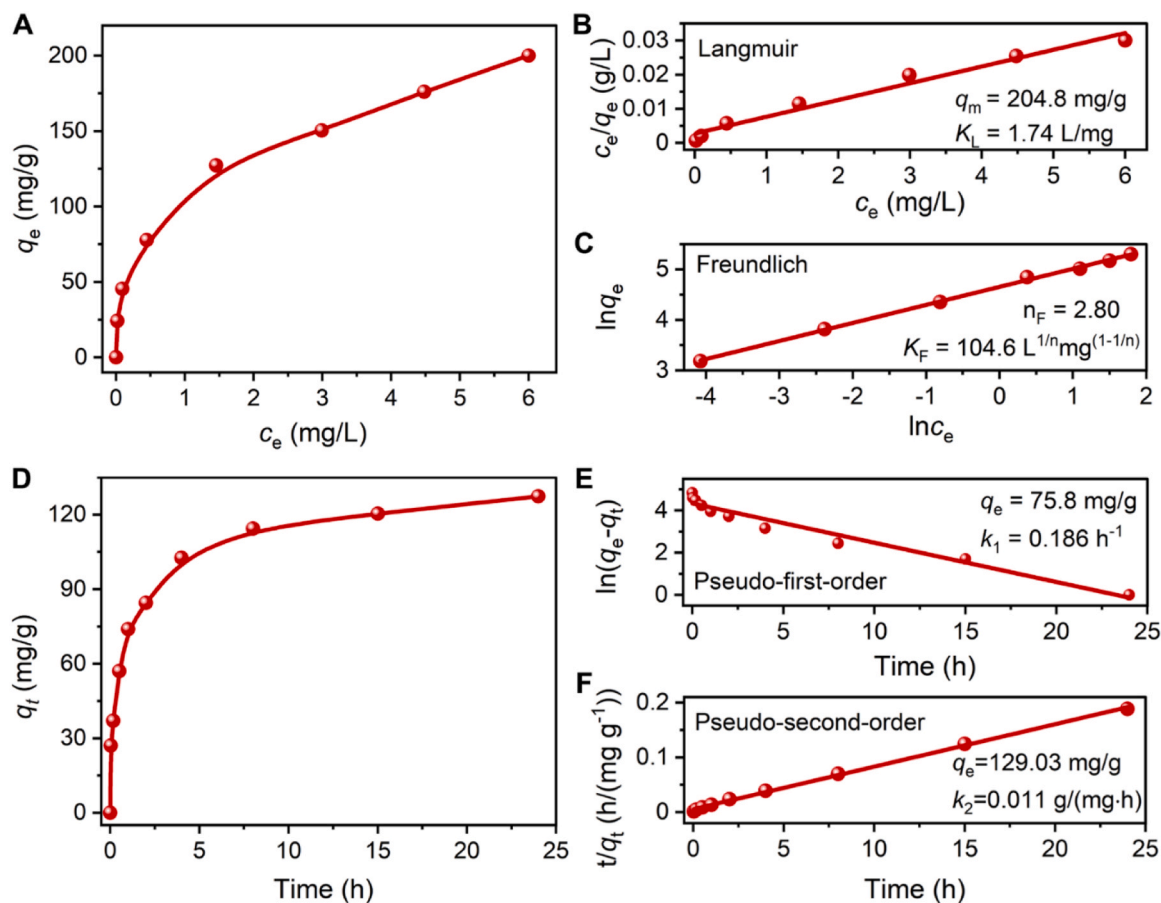


Fig. 3. (A) An adsorption isotherm of tetracycline on Fe@CNO at a fixed Fe@CNO concentration of 20 mg/L in aqueous solution, (B) Langmuir and (C) Freundlich model, fitting of tetracycline adsorption on Fe@CNO, using data from (A). (D) Adsorption kinetic data of 4 mg/L tetracycline adsorption on 20 mg/L Fe@CNO in aqueous solution. (E) pseudo-first-order and (F) pseudo-second-order fittings of kinetic data from (D).

Fig. 3A shows an upward trend at the c_e of 6.01 mg/L, suggesting that the adsorption capacity can be increased further if tetracycline's initial concentration is higher [59].

The mechanism for tetracycline adsorption on graphite surfaces is still not fully understood in previous studies [60–62]. The tetracycline is an amphoteric molecule with three pK_a values at 3.3, 7.7, and 9.7 and forms a series of functional groups at different pH. The predominant species are H_4TC^+ at $pH < 3.4$, H_3TC at $3.4 < pH < 7.6$, H_2TC^- at $7.6 < pH < 9.7$, and HTC^{2-} at $pH > 9.7$, respectively [63]. Carbon materials with negative surface potentials have the maximum tetracycline adsorption capacity when pH is around 6–7 [63,64]. In this study, the pH of the tetracycline solution is around 6.3, and Fe@CNO has a negative surface potential at this pH (see the zeta-potential of Fe@CNO measured in water in Fig. S3 in the Supporting Information). Thus, the high adsorption capacity of tetracycline on Fe@CNO may be attributed to several types of interactions, including hydrogen bonding, π - π electron donor-acceptor interactions, and cation- π bonding [65,66].

Fig. 3D shows the adsorption kinetic data at the initial tetracycline concentration of 4 mg/L. About 60% of the total adsorption capacity was achieved during a rapid adsorption period in the first 2 h. The kinetic data were fitted with pseudo-first-order and pseudo-second-order models (see details in the Experimental Section). The fitting results are presented in Fig. 3E, F, and Table S2 in the Supporting Information. The pseudo-second-order model fits the data well with $R^2 \geq 0.99$, similar to previous studies of tetracycline adsorption on solid adsorbents [63], such as kaolinite [67], graphene oxide [66], and montmorillonite [68].

3.3. H_2O_2 synthesis using Fe@CNO-O electrocatalysts

Previous studies have demonstrated that oxidized carbon materials are efficient electrocatalysts for H_2O_2 via 2-electron-transfer ORR [37, 38,40–47]. Fe@CNO-O electrocatalysts were prepared by chemical

oxidation of Fe@CNO using concentrated HNO_3 for 1, 3, and 6 h, as described in the Experimental Section. They were denoted as Fe@CNO-O-1, Fe@CNO-O-3, and Fe@CNO-O-6, respectively. Their TEM images and XRD patterns in Fig. 4A and B demonstrate that oxidation does not significantly affect the graphitic crystallinity of CNO. However, TEM images in Fig. S4 and TGA profiles in Fig. S5 in the Supporting Information show that a significant fraction of Fe particles encapsulated by CNO have been removed after HNO_3 oxidation. XPS spectra in Fig. 4C show that the intensity of the O peak from Fe@CNO-O increases significantly, indicating the formation of oxygen functional groups on CNO surfaces. Raman spectra in Fig. 4D reveal that the intensity ratio between D and G band peaks increases from 0.4 to 0.49 after oxidation, indicating that the oxidation creates defects in CNO shells.

The catalytic performance of Fe@CNO and Fe@CNO-O for ORR was first evaluated using RRDEs in 0.05 M Na_2SO_4 aqueous electrolyte at a pH of 7 (adjusted by phosphate-buffered saline (PBS) in a three-electrode configuration (see details in the Experimental Section). Fig. 5A shows that Fe@CNO-O-3 delivers a much higher ring current than Fe@CNO, indicating the highest H_2O_2 production rate. Fig. 5B shows that the ORR selectivity towards H_2O_2 production (see the calculation method in the Experimental Section) is the highest at 80% on Fe@CNO-O-3 compared to 50% on Fe@CNO. Fe@CNO-O-3 performs best among the three Fe@CNO-O electrocatalysts. Fig. S6 in the Supporting Information shows that Fe@CNO-O-3 delivers the lowest electron transfer number, consistent with the selectivity calculated. We also compared the three Fe@CNO-O electrocatalysts in 0.05 M Na_2SO_4 aqueous electrolytes at pH 3 and 10. Fig. S7 in the Supporting Information shows that all three Fe@CNO-O electrocatalysts are active for $2e^-$ ORR in the acidic and basic electrolytes. Overall, Fe@CNO-O-3 delivers the optimum performance under all three pH conditions.

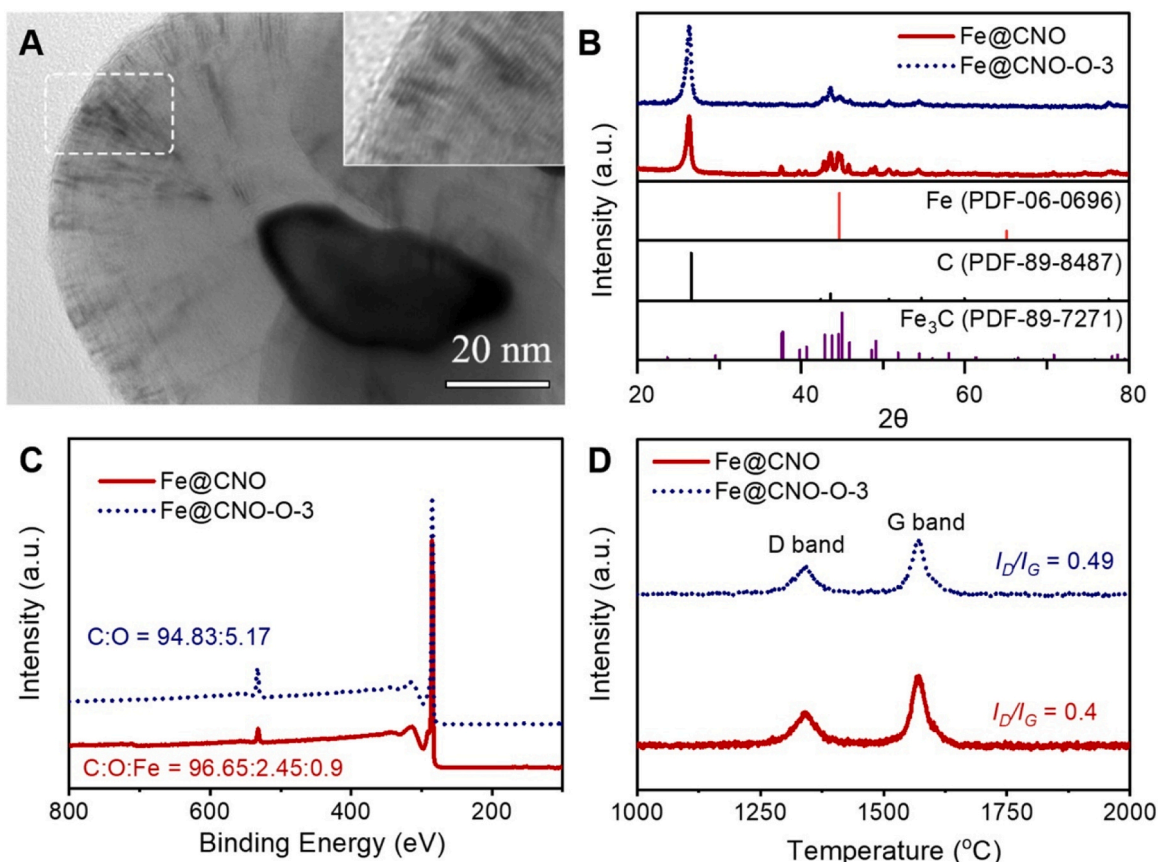


Fig. 4. Physicochemical characterizations of Fe@CNO and Fe@CNO-O-3. (A) TEM images, (B) XRD patterns, (C) XPS spectra, (D) Raman spectra.

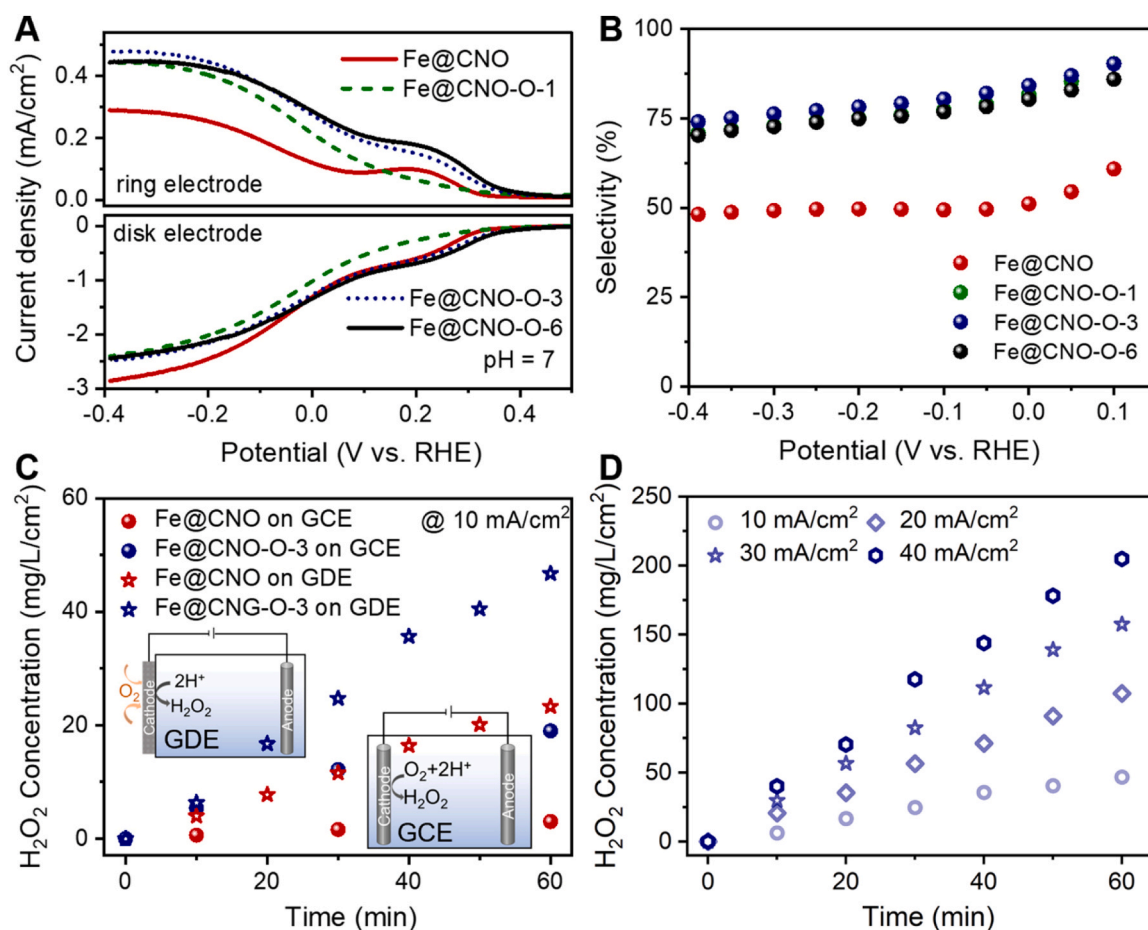


Fig. 5. Comparison of electrocatalytic performance of Fe@CNO and Fe@CNO-O for 2e⁻ ORR. (A) ORR polarization curves of the disk electrode and the ring electrode at 1600 rpm in 0.05 M Na₂SO₄ at pH of 7 adjusted using PBS, (B) the corresponding ORR selectivity toward H₂O₂ from (A). (C) The H₂O₂ concentration produced in 100 mL 0.05 M Na₂SO₄ electrolyte using Fe@CNO and Fe@CNO-O-3 loaded on GCEs and GDEs as cathodes with the mass loading of 5 mg/cm² at the current density of 10 mA/cm². The insets show the schematic illustrations of two-electrode electrolyzers using the GDE cathode (left) and the GCE cathode (right). (D) The H₂O₂ concentration using Fe@CNO-O-3 loaded on GDEs as cathodes in two-electrode electrolyzers at different applied current densities from 10 to 40 mA/cm².

Because the H₂O₂ production via ORR is often limited by low solubility and slow mass transfer of O₂ in water [69,70], we speculated that GDEs would allow more efficient O₂ mass transfer from air to active catalytic sites. Thus, we deposited Fe@CNO or Fe@CNO-O-3 on carbon cloth with a mass loading of 5 mg/cm² to form GDEs with the size of 12 cm² (see Experimental section for the detail of electrode fabrication). As illustrated in the left inset of Fig. 5C, H₂O₂ production performance was compared using the two-electrode electrolyzer containing 100 mL 0.05 M Na₂SO₄ electrolyte. The targeted 2e⁻ ORR occurred on the GDE cathode containing Fe@CNO or Fe@CNO-O-3, coupled with water oxidation to produce O₂ at the anode containing commercial IrO₂ electrocatalysts (2.5 mg/cm²) deposited on Ti mesh (12 cm²). Fe@CNT and Fe@CNO-O-3 were also deposited on standard glassy carbon electrodes (GCEs) with the same mass loading of 5 mg/cm² for comparison, as illustrated in the right inset of Fig. 5C. Fig. 5C shows the concentration of H₂O₂ produced after different reaction periods at the current density of 10 mA/cm². Fe@CNO deposited on GCE only produces 3.0 mg/L/cm² H₂O₂ in 60 min. In comparison, Fe@CNO-O-3 deposited on GCE produces 6 times more H₂O₂ of 19.1 mg/L/cm² in 60 min. H₂O₂ production from Fe@CNO deposited on GDE is 23.3 mg/L/cm², much higher than from Fe@CNO deposited on GCE. Fe@CNO-O-3 deposited on GDE further doubles H₂O₂ production to 46.7 mg/L/cm², also much higher Fe@CNO-O-3 deposited on GCE. Furthermore, Fig. 4D shows that the current density applied on Fe@CNO-O-3 deposited on GDE can be increased to 40 mA/cm², leading to the H₂O₂ production of

204 mg/L/cm² in 60 min. We also compared the H₂O₂ production yield at the three pH conditions (i.e., 3, 7, and 10) under the applied current density of 40 mA/cm², as shown in Fig. S8 in the Supporting Information. The H₂O₂ production yield is similar under the three pH conditions in the first 20 min. However, the H₂O₂ concentration in the electrolyte at the pH of 10 drops after 20 min may be due to the self-decomposition of H₂O₂ in basic electrolytes. Notably, a high H₂O₂ production yield can be obtained in the neutral condition.

Previous studies have shown that the catalytic performance of oxidized carbon nanotubes or partially reduced graphene oxide for H₂O₂ synthesis depends on their surface O content [71,72]. Defects in carbon materials can promote O adsorption during ORR, increasing H₂O₂ synthesis [40]. Further, ORR electrocatalysts' surface wettability can often influence their performance. The oxidation of HNO₃ can change the surface O content, defects, and surface wettability of Fe@CNO-O. To better understand the catalytic behaviors of Fe@CNO-O, we characterized them by XPS, SEM, ICP-OES, TGA, and magnetization measurement. The results are presented in Figs. S9, S10, S11 and Table S3 in the Supporting Information. XPS spectra in Fig. S9A show that the O content increases from 2.45% in Fe@CNO to 2.99% in Fe@CNO-O-1, 5.17% in Fe@CNO-O-3, and 8.77 at% in Fe@CNO-O-6. The XPS C 1s spectra in Fig. S9B were deconvoluted into five peaks: C in graphite (C-C sp²) at 284.5 eV, C in defects (C-C sp³) at 285.4 eV, C singly bound to O (C-O) at 286.1 eV, C bound to two O (-O-C=O) at 288.7 eV, and C in aromatic compounds (π - π^* transition) at 290.5 eV [71]. The area of the

deconvoluted C peaks in defects increases with oxidation time. SEM elemental mappings of Fe@CNO and Fe@CNO-O-3 in Fig. S10 show a similar trend in the O content change. It should be noted that N can not be easily doped into graphitic carbon materials by HNO₃ oxidation [71]. Both XPS and SEM detected no N species. ICP-OES analysis shows that the Fe and Al are only 1.2 and 0.014 wt% in Fe@CNO-O-3, respectively. The significantly lower Fe and Al contents indicate that most exposed metal species have been removed by HNO₃ oxidation. However, TGA results in Fig. S11A show that there are still 7 wt% residues in Fe@CNO-O are metal species encapsulated by thick graphitic layers. Further, there is a significant decrement of magnetization in Fe@CNO-O (3.7 emu/g) compared to Fe@CNO (28 emu/g). The remaining magnetization should come from encapsulated Fe particles. Since these encapsulated metal particles cannot be removed by HNO₃ oxidation, they are unlikely to contribute to H₂O₂ production.

Photos in Fig. S12 in the Supporting Information display that the water contact angles on Fe@CNO-O decrease from 112° to 95°, indicating increased electrocatalyst surface hydrophilicity. Fig. S13A in the Supporting Information shows that the H₂O₂ production yield is the highest on Fe@CNO-O-3. If we correlate the H₂O₂ production yield with O content and C defects in Fe@CNO-O (Fig. S13B and C), the higher O content and defect density in Fe@CNO-O-6 lead to a lower H₂O₂ production yield. We propose that this can be attributed to the higher surface wettability of Fe@CNO-O-6 (Fig. S12). When liquid electrolytes fully cover the hydrophilic electrode surface, the efficient mass transfer of gaseous O₂ to active catalytic sites could be compromised. Overall, Fe@CNO-O-3 is the optimum electrocatalyst for H₂O₂ synthesis.

We also calculated the electrolyzer's electrical energy consumption and current efficiency at different current densities (see Experimental Section for the calculation method). The results in Fig. S14 in the Supporting Information show that less electricity (3.85 kWh) is required to produce 1 kg of H₂O₂ at 10 mA/cm² than at 40 mA/cm² (8.98 kWh). The current dominant industrial H₂O₂ production process by the anthraquinone cycling would consume 8.1 kWh to produce 1 kg of H₂O₂ without considering the cost of H₂/O₂ feedstocks [73]. The total operating cost for H₂O₂ production by the electrocatalytic synthesis method includes electricity and electrolyte costs [47]. Assuming the electrolyte would not be reused, Fig. S15 in the Supporting Information shows that the total cost is lower at the current density of 40 mA/cm². Overall, the electrocatalytic synthesis of H₂O₂ using Fe@CNO-O-3 deposited on GDE is cost-effective.

3.4. The degradation of concentrated tetracycline in the electro-Fenton process

Next, Fe@CNO saturated with tetracycline collected from the solid/liquid separation was treated in the electro-Fenton process (see Fig. 1). A single-compartment two-electrode electrolyzer was filled with 0.05 M Na₂SO₄ electrolyte. The Fe@CNO-O-3 deposited on carbon cloth served as its GDE cathode, and IrO₂ electrocatalysts on Ti mesh served as its anode. Due to the higher mass transfer resistance at a lower concentration, degrading organic contaminants at a higher initial concentration would be a more efficient approach [74,75]. Thus, we first explored the suitable initial tetracycline concentration. The initial tetracycline

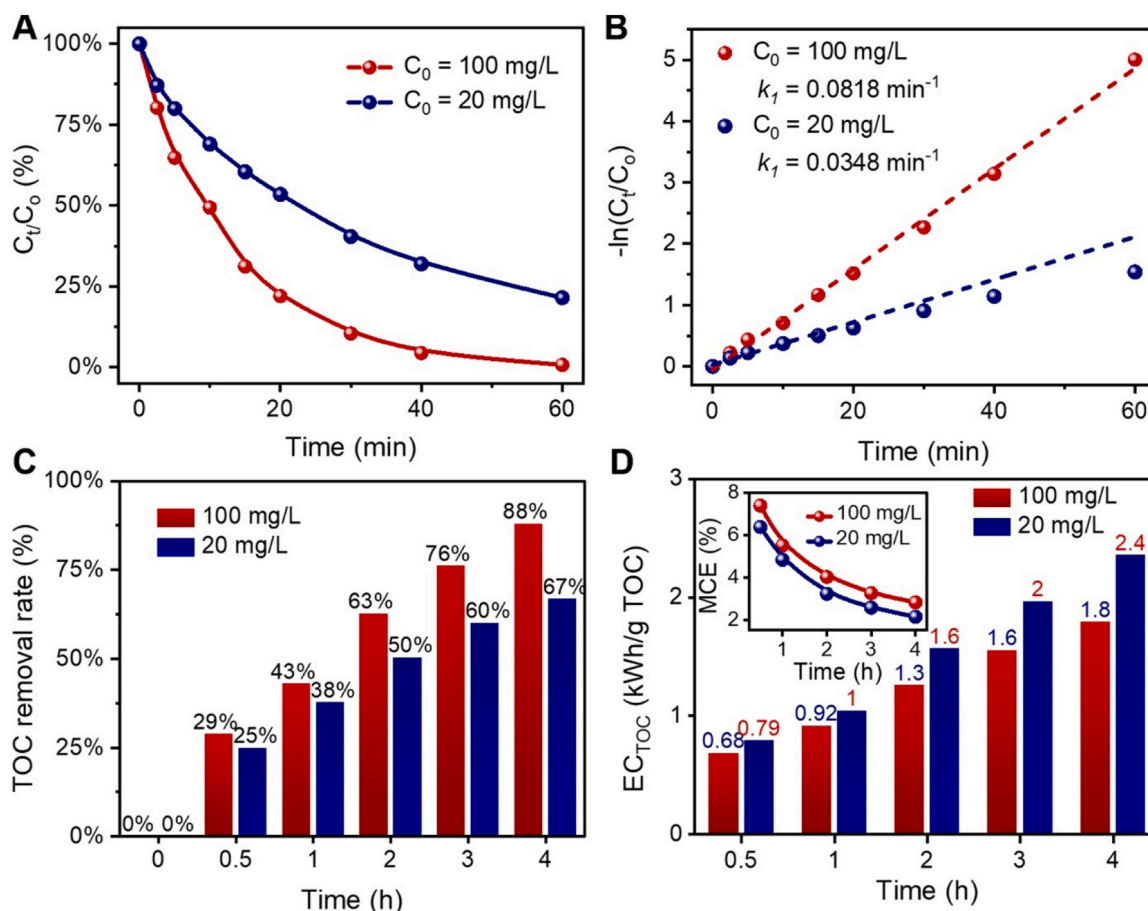


Fig. 6. Tetracycline degradation in the electro-Fenton process with integrated in situ H₂O₂ generation at the applied current density of 40 mA/cm² on the Fe@CNO-O-3 GDE cathode and the electrolyte pH of 7. (A) The degradation efficiency of tetracycline at two initial tetracycline concentrations (C₀) in 60 min; (B) the first-order kinetic modeling of the tetracycline degradation based on data in (A); (C) TOC removal rate at the two initial tetracycline concentrations in the 4 h, and (D) the corresponding energy consumption (EC_{TOC}) and mineralization current efficiency (MCE).

concentration was adjusted by adding different amounts of saturated Fe@CNO based on its approximate adsorption capacity of 200 mg/g. Fig. 6A compared the tetracycline removal efficiency at two initial tetracycline concentrations (i.e., 20 and 100 mg/L) in the first 60 min. The corresponding Fenton catalyst (Fe@CNO) concentration at these two conditions was 100 and 500 mg/L, respectively. We also set the total amount of tetracycline the same in these two conditions; hence, the entire electrolyte volume was 500 mL for the tetracycline concentration of 20 mg/L and 100 mL for the tetracycline concentration of 100 mg/L. The removal efficiency is higher when the initial tetracycline concentration is higher, with 100% removal in 60 min (Fig. 6A) and a higher reaction rate at 0.818 min^{-1} based on the first-order reaction kinetics (Fig. 6B). When the reaction time was extended for 4 h, the mineralization efficiency was 88% and 67% by TOC analysis at the two initial tetracycline concentrations, respectively (Fig. 6C). The effect of the initial concentration on TOC removal was further analyzed based on the specific energy consumption of removing 1 kg TOC (EC_{TOC}) and the MCE (Fig. 6D). Lower energy was consumed to mineralize 1 kg TOC with a higher MCE when the initial concentration was higher. EC_{TOC} gradually increased, and MCE gradually decreased when the electrolysis time was prolonged. The limited mass transfer may explain this due to the decreasing organic content concentration. From the above results, we concluded that tetracycline degradation is more efficient at the higher initial concentration of 100 mg/L than at 20 mg/L.

We further optimized the pH of the electrolyte and the applied

current density on cathodes. In standard homogenous Fenton reaction processes, the optimum pH is in a relatively narrow range of 2.8–3.5. Fig. S16A in the Supporting Information shows that the electro-Fenton process based on in situ H_2O_2 generation and tetracycline-saturated Fe@CNO can work efficiently in a wide pH range from 3 to 10. Under the pH of 3, the reaction rate is 0.106 min^{-1} according to the first-order reaction kinetics, while the reaction rate is even higher at 0.210 min^{-1} at a pH of 10 (Fig. S16B). Because of the more complex operational procedures and additional costs involved in adjusting the pH of the electrolyte, an electro-Fenton process operated at a pH of 7 is preferred, which can provide a sufficiently high reaction rate of 0.0818 min^{-1} . Furthermore, upon the complete degradation of adsorbed tetracycline, Fe@CNO was regenerated, which was reused in the next adsorption cycle.

3.5. Reaction mechanism of the electro-Fenton process

The degradation of tetracycline in the electro-Fenton process may be related to several reactions, including heterogeneous Fenton reaction on Fe@CNO, direct electrochemical oxidation by H_2O_2 generated on the cathode, and direct oxidation by $\bullet\text{OH}$ generated on the anode [76]. Several control experiments were carried out to understand the contributions of these reactions. First, we directly added tetracycline into the 0.05 M Na_2SO_4 electrolyte without adding Fe@CNO. The process was denoted as electrochemical oxidation. Next, we used an ion exchange

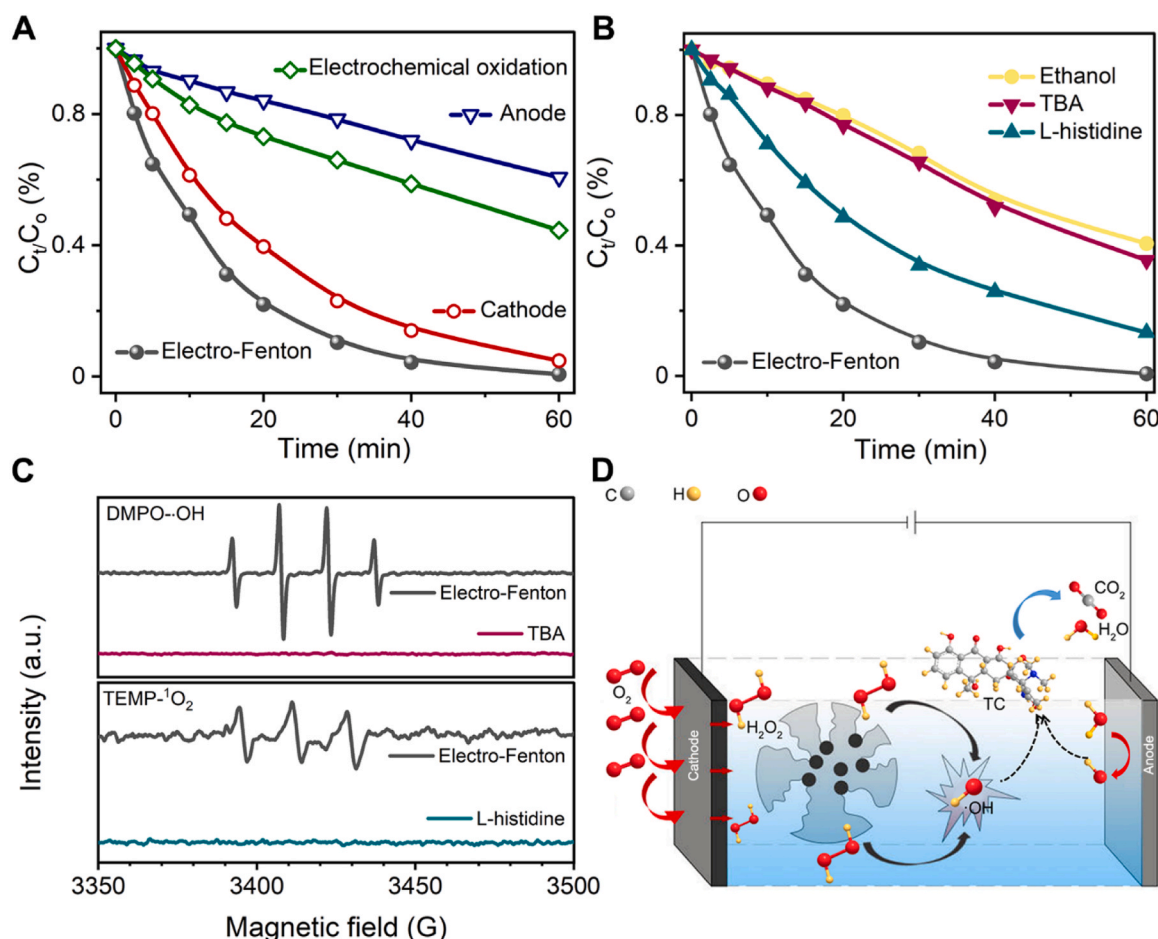


Fig. 7. (A) Comparison of tetracycline removal efficiency in the electro-Fenton process using the single-compartment two-electrode electrolyzer with or without adding Fe@CNO (denoted as electrochemical oxidation) and in a two compartments electrolyzer separated by an ion exchange membrane. The initial tetracycline concentration is 100 mg/L, the current density is 40 mA/cm^2 , and the pH of 0.05 M Na_2SO_4 electrolyte is 7. (B) The changes of tetracycline removal efficiency in the electro-Fenton in the electro-Fenton process upon adding different oxidative radical scavengers, including methanol, TBA, and L-histidine, at 200 mM. (C) EPR spectra of DMPO- $\bullet\text{OH}$ and TEMP- $^1\text{O}_2$. (D) A schematic illustration of the reaction mechanism of Fe@CNO in the electro-Fenton process.

membrane to divide the single-chamber electrolyzer into anode and cathode chambers. Fe@CNO saturated with tetracycline was equally divided into the two chambers, and the degradation of tetracycline in these two chambers was quantified separately. Fig. 7A shows that the electrochemical oxidation has a degradation efficiency of 55.7%, much lower than the electro-Fenton process, indicating the critical role of Fe@CNO as a heterogeneous Fenton catalyst. The degradation efficiency in the anode chamber of the electro-Fenton process is 39.04%, much lower than 95.2% in the cathode chamber, suggesting that direct oxidation by $\bullet\text{OH}$ generated on the anode plays a minor role. First-order kinetic modeling of these control experiments shows the same trend (Fig. S17 in the Supporting Information). Overall, the electro-Fenton process catalyzed by the Fe@CNO heterogeneous Fenton catalyst is the main contributor to the tetracycline degradation.

Next, we further explored the reaction mechanism by free radical quenching experiments. Although $\bullet\text{OH}$ is the most frequently cited active species in electro-Fenton processes, several other strong oxidizing species, such as $\bullet\text{SO}_4$, Fe (IV), and $^1\text{O}_2$, may also be present. Thus, several scavengers (listed in Table S4 in the Supporting Information), including methanol ($\bullet\text{OH}$ and $\bullet\text{SO}_4$), *tert*-butyl alcohol (TBA, $\bullet\text{OH}$ scavenger), and L-histidine ($^1\text{O}_2$ scavenger), were added to the electrolyte in the free radical quenching experiments. Fig. 7B shows that methanol and TBA have similar inhibition on the tetracycline removal, suggesting the significant role of $\bullet\text{OH}$ and the negligible role of $\bullet\text{SO}_4$ generated at the anode. When L-histidine was added to quench $^1\text{O}_2$, the tetracycline removal only showed a slight decrease, reaching 86.8% in 60 min. First-

order kinetic modeling of these free radical quenching experiments shows the same trend (Fig. S18 in the Supporting Information).

The existence of free radicals was further confirmed by using EPR. Fig. 7C shows 4-fold peaks of DMPO- $\bullet\text{OH}$ adducts with an intensity ratio of 1:2:2:1 and weakened triplet signals of TEMP- $^1\text{O}_2$. However, no DMPO- $\bullet\text{SO}_4$ signals were detected. EPR results are consistent with the quenching experiments. No specific signals were detected in the presence of scavengers. Thus, we conclude that $\bullet\text{OH}$ is the main oxidative species responsible for tetracycline removal.

In summary, the mechanism of degradation of tetracycline in the electro-Fenton process is illustrated in Fig. 7D. O_2 in the air diffuses through the GDE and is reduced to H_2O_2 through 2e^- ORR on the oxidized Fe@CNO in the cathode. C-C sp^3 defects in oxidized Fe@CNO may promote O_2 adsorption, and its porous structure is also beneficial for O_2 transport and trapping. Next, in situ synthesized H_2O_2 is activated to $\bullet\text{OH}$ by Fe@CNO. Part of the generated $\bullet\text{OH}$ may be released into the bulk solution, and some are still adsorbed on the surface of Fe@CNO. Both $\bullet\text{OH}$ attack tetracycline, degrade it into intermediates and finally mineralize them into CO_2 and H_2O . The direct oxidation by $\bullet\text{OH}$ generated on the anode plays a minor role in tetracycline degradation.

3.6. Performance stability and degradation of organic pollutants in different water matrices

The stability and reusability of Fenton catalysts are essential for practical applications. We carried out consecutive experiments for 5

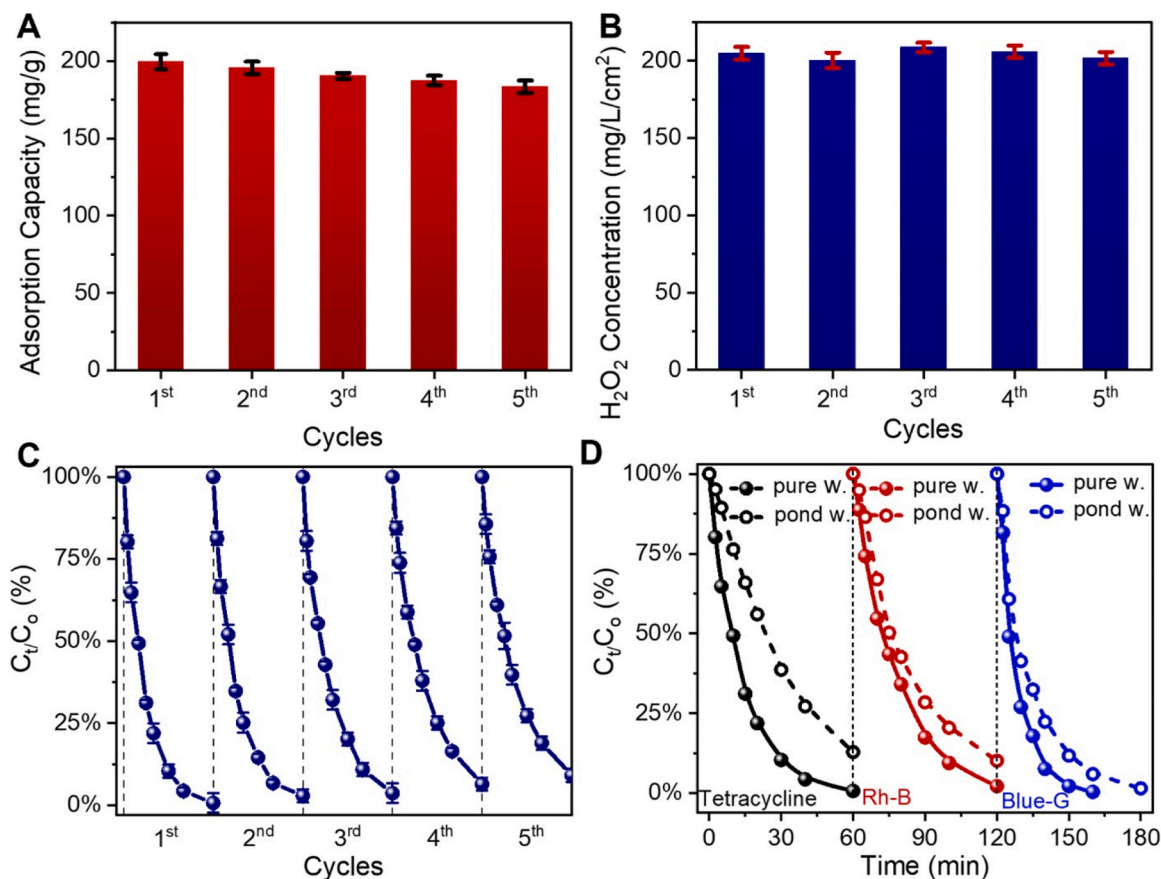


Fig. 8. Stability of Fe@CNO as a trifunctional catalyst/adsorbent for wastewater treatment in five continuous cycles. (A) The adsorption capacity of tetracycline on Fe@CNO in the five cycles at a fixed Fe@CNO concentration of 20 mg/L, (B) H_2O_2 production yield on Fe@CNO-O-3 loaded on GDE as cathodes with the mass loading of 5 mg/cm² at the current density of 40 mA/cm² in five cycles. (C) The tetracycline removal efficiency in five cycles under the same condition used in Fig. 6 at the initial tetracycline concentration of 100 mg/L and treatment of 60 min at the applied current density of 40 mA/cm² for each cycle; (D) Degradation of different organic pollutants in two different water matrices at the applied current density of 40 mA/cm². The initial organic contaminant concentrations are C_0 , tetracycline = 100 mg/L, C_0 , Rh-B = 8 mg/L, C_0 , Blue G = 6.8 mg/L at pH of 7. The Rh-B and Blue G initial concentrations are set based on their adsorption capacity on Fe@CNO of $q_{\text{Rh-B}} = 16$ mg/g, $q_{\text{Blue G}} = 13.6$ mg/g, respectively.

continuous cycles to evaluate the performance stability of the new process. Fig. 8A–C show that the adsorption capability, the H_2O_2 production yield, and the tetracycline degradation efficiency remain stable over the 5 cycles, respectively. Fe@CNO can be effectively regenerated in the electro-Fenton process and reused in the next adsorption cycle with a similar capability. These results indicate the high potential for achieving excellent reusability.

Two other organic pollutants, Rhodamine B (Rh-B) and Brilliant Blue-G (Blue-G), were selected and tested in comparison to tetracycline in two water matrices, including pure water and natural water from a local pond, to explore further the potential to treat various organic contaminants. There are various natural organic matters (NOMs) in the natural water, such as humic acid and fulvic acid. The roles of these NOMs are complex. They may serve as a radical quencher, active site occupier, and/or electron transfer mediator [77]. Fig. 8D shows that all the pollutants' removal efficiency in pure water is higher than 99.5% within 60 min. In comparison, in natural water, the electro-Fenton process can still efficiently degrade the target contaminants with some reduction in the removal efficiency because of the interruptions of other organics in the water. The removal efficiency is still higher than 95%, also confirmed by TOC tests.

4. Conclusions

In summary, we demonstrate that Fe@CNO is a highly efficient tri-functional adsorbent and catalyst for degrading organic contaminants. Fe@CNO shows an adsorption capacity of 199.5 mg/g at the equilibrium tetracycline concentration of 6.01 mg/L. 60% of the adsorption capacity is reached in the first 2 h. The homogeneous monolayer adsorption at low tetracycline concentrations shifts into heterogeneous multilayer adsorption with increased initial tetracycline concentration, following a pseudo-second-order kinetic model. Further, Fe@CNO saturated with tetracycline can be easily separated from water under an external magnetic field. Fe@CNO-O-3 obtained after refluxing in HNO_3 for 3 h is a highly active electrocatalyst for H_2O_2 synthesis in acidic, basic, and neutral electrolytes. Fe@CNO-O-3 (5 mg/cm²) deposited on GDEs deliver H_2O_2 production of 204 mg/L/cm² in 1 h under at the current density of 40 mA/cm². Considering the total cost of electricity and electrolyte consumed, a two-electrode electrolyzer, using Fe@CNO-O-3 deposited on GDE as a cathode and IrO_2/Ti mesh as an anode can produce H_2O_2 more cost-effectively than the existing dominant industrial H_2O_2 production process by the anthraquinone cycling. When the electrolyzer is applied to treat tetracycline concentrated on Fe@CNO, Fe@CNO serves as an efficient heterogeneous Fenton catalyst. 100% of tetracycline (100 mg/L) is degraded in 1 h, following the first-order reaction kinetics at a reaction rate of 0.0818 min⁻¹. The tetracycline's mineralization efficiency is 88% in 4 h by TOC analysis. This electro-Fenton process can work efficiently in a wide pH range from 3 to 10. Mechanism studies show that the electro-Fenton process catalyzed by Fe@CNO is the main contributor to tetracycline degradation. $\bullet\text{OH}$ is the main oxidative species responsible for tetracycline degradation, while direct oxidation by $\bullet\text{OH}$ generated on the anode only plays a minor role. Fe@CNO can also be regenerated in the electro-Fenton process, separated from water under an external magnetic field, and reused in the next adsorption cycle with a similar capability, as demonstrated in 5 continuous cycles. It also applies to various organic pollutants in different water matrices, such as Rh-B and Blue-G. This work provides a new strategy to sustainably utilize carbon co-products from CH_4 pyrolysis, which opens the door to integrate clean H_2 production with environmental applications.

CRediT authorship contribution statement

Yuanyuan Yao: Conceptualization, Methodology, Formal analysis, Writing – original draft. **Yuqi Pan:** Methodology, Data curation, Investigation. **Leo Lai:** Methodology, Formal analysis. **Zixun Yu:** Data

curation, Formal analysis. **Jiaxiang Chen:** Methodology, Formal analysis. **Yanxi Yu:** Methodology, Resources, Formal analysis. **Terrence Darma:** Methodology. **Yongwen Tao:** Data curation, Methodology. **Liuyue Cao:** Methodology, Validation. **Benjamin Chivers:** Writing – review & editing. **Li Wei:** Methodology, Writing – review & editing. **Yuan Chen:** Conceptualization, Supervision, Funding acquisition, Project administration, Writing – review & editing.

Declaration of Competing Interest

The authors declare that they have no known competing financial interests or personal relationships that could have appeared to influence the work reported in this paper.

Data availability

Data will be made available on request.

Acknowledgments

This study was co-funded by the Australian Government Department of Industry, Science, Energy and Resource (Innovative Manufacturing Cooperative Research Centre).

Appendix A. Supporting information

Supplementary data associated with this article can be found in the online version at doi:10.1016/j.apcatb.2023.123380.

References

- [1] C. Pratt, K. Tate, Mitigating methane: emerging technologies to combat climate change's second leading contributor, *Environ. Sci. Technol.* 52 (2018) 6084–6097.
- [2] B. Parkinson, P. Balcombe, J.F. Speirs, A.D. Hawkes, K. Hellgardt, Levelized cost of CO_2 mitigation from hydrogen production routes, *Energy Environ. Sci.* 12 (2019) 19–40.
- [3] A. Kumar, Ethanol decomposition and dehydrogenation for hydrogen production: a review of heterogeneous catalysts, *Ind. Eng. Chem. Res.* 60 (2021) 16561–16576.
- [4] O. Machhammer, A. Bode, W. Hormuth, Financial and ecological evaluation of hydrogen production processes on large scale, *Chem. Eng. Technol.* 39 (2016) 1185–1193.
- [5] B. Lumbers, J. Barley, F. Platte, Low-emission hydrogen production via the thermocatalytic decomposition of methane for the decarbonisation of iron ore mines in Western Australia, *Int. J. Hydrog. Energy* 47 (2022) 16347–16361.
- [6] A. Konieczny, K. Mondal, T. Wiltowski, P. Dydo, Catalyst development for thermocatalytic decomposition of methane to hydrogen, *Int. J. Hydrog. Energy* 33 (2008) 264–272.
- [7] A.F. Cunha, J.J.M. Órfão, J.L. Figueiredo, Methane decomposition on Ni–Cu alloyed Raney-type catalysts, *Int. J. Hydrog. Energy* 34 (2009) 4763–4772.
- [8] D. Torres, S. de Llobet, J.L. Pinilla, M.J. Lázaro, I. Suelves, R. Moliner, Hydrogen production by catalytic decomposition of methane using a Fe-based catalyst in a fluidized bed reactor, *J. Nat. Gas Chem.* 21 (2012) 367–373.
- [9] D. Torres, J.L. Pinilla, I. Suelves, Cobalt doping of $\alpha\text{-Fe}/\text{Al}_2\text{O}_3$ catalysts for the production of hydrogen and high-quality carbon nanotubes by thermal decomposition of methane, *Int. J. Hydrog. Energy* 45 (2020) 19313–19323.
- [10] M. Caban, P. Stepnowski, How to decrease pharmaceuticals in the environment? A review, *Environ. Chem. Lett.* 19 (2021) 3115–3138.
- [11] L. Dsikowitzky, J. Schwarzbauer, Industrial organic contaminants: identification, toxicity and fate in the environment, *Environ. Chem. Lett.* 12 (2014) 371–386.
- [12] J.J. Pignatello, E. Oliveros, A. MacKay, Advanced oxidation processes for organic contaminant destruction based on the Fenton reaction and related chemistry, *Crit. Rev. Environ. Sci. Technol.* 36 (2006) 1–84.
- [13] X. Liu, H. Yu, J. Ji, Z. Chen, M. Ran, J. Zhang, M. Xing, Graphene oxide-supported three-dimensional cobalt–nickel bimetallic sponge-mediated peroxymonosulfate activation for phenol degradation, *ACS ES&T Eng.* 1 (2021) 1705–1714.
- [14] Y. Liu, Y. Zhao, J. Wang, Fenton/Fenton-like processes with in-situ production of hydrogen peroxide/hydroxyl radical for degradation of emerging contaminants: advances and prospects, *J. Hazard. Mater.* 404 (2021), 124191.
- [15] B.C. Hodges, E.L. Cates, J.-H. Kim, Challenges and prospects of advanced oxidation water treatment processes using catalytic nanomaterials, *Nat. Nanotechnol.* 13 (2018) 642–650.
- [16] J. Lee, U. von Gunten, J.H. Kim, Persulfate-based advanced oxidation: critical assessment of opportunities and roadblocks, *Environ. Sci. Technol.* 54 (2020) 3064–3081.
- [17] Y. Su, K.X. Fu, C.H. Pang, Y.F. Zheng, C.F. Song, N. Ji, D.G. Ma, X.B. Lu, C.X. Liu, R. Han, Q.L. Liu, Recent advances of chlorinated volatile organic compounds'

- oxidation catalyzed by multiple catalysts: reasonable adjustment of acidity and redox properties, *Environ. Sci. Technol.* 56 (2022) 9854–9871.
- [18] Z. Wang, W. Qiu, S.Y. Pang, Q. Guo, C.T. Guan, J. Jiang, Aqueous iron(IV)-oxo complex: an emerging powerful reactive oxidant formed by iron(II)-based advanced oxidation processes for oxidative water treatment, *Environ. Sci. Technol.* 56 (2022) 1492–1509.
 - [19] L. Tian, P. Chen, X.-H. Jiang, L.-S. Chen, L.-L. Tong, H.-Y. Yang, J.-P. Fan, D.-S. Wu, J.-P. Zou, S.-L. Luo, Mineralization of cyanides via a novel Electro-Fenton system generating $\bullet\text{OH}$ and $\bullet\text{O}_2^-$, *Water Res.* 209 (2022), 117890.
 - [20] H. Gallard, J. de Laat, B. Legube, Influence du pH sur la vitesse d'oxydation de composés organiques par $\text{Fe}^{3+}/\text{H}_2\text{O}_2$. Mécanismes réactionnels et modélisation, *New J. Chem.* 22 (1998) 263–268.
 - [21] M.A. Oturan, J. Peiroten, P. Chartrin, A.J. Acher, Complete destruction of p-nitrophenol in aqueous medium by Electro-Fenton method, *Environ. Sci. Technol.* 34 (2000) 3474–3479.
 - [22] N. Oturan, M. Panizza, M.A. Oturan, Cold incineration of chlorophenols in aqueous solution by advanced electrochemical process Electro-Fenton effect of number and position of chlorine atoms on the degradation kinetics, *J. Phys. Chem. A* 113 (2009) 10988–10993.
 - [23] I. Sirés, E. Brillas, M.A. Oturan, M.A. Rodrigo, M. Panizza, Electrochemical advanced oxidation processes: today and tomorrow. A review, *Environ. Sci. Pollut. Res.* 21 (2014) 8336–8367.
 - [24] Y. Lin, P. Huo, F. Li, X. Chen, L. Yang, Y. Jiang, Y. Zhang, B.-J. Ni, M. Zhou, A critical review on cathode modification methods for efficient Electro-Fenton degradation of persistent organic pollutants, *Chem. Eng. J.* 450 (2022), 137948.
 - [25] W. Zhou, X. Meng, J. Gao, A.N. Alshawabkeh, Hydrogen peroxide generation from O_2 electroreduction for environmental remediation: a state-of-the-art review, *Chemosphere* 225 (2019) 588–607.
 - [26] K.M. Nair, V. Kumaravel, S.C. Pillai, Carbonaceous cathode materials for electro-Fenton technology: mechanism, kinetics, recent advances, opportunities and challenges, *Chemosphere* 269 (2021), 129325.
 - [27] L. Li, J. Li, F. Fang, Y. Zhang, T. Zhou, C. Zhou, J. Bai, B. Zhou, Efficient H_2O_2 production from urine treatment based on a self-biased WO_3/TiO_2 -Si PVC photoanode and a $\text{WO}_3/\text{CMK-3}$ cathode, *Appl. Catal. B Environ.* 333 (2023), 122776.
 - [28] A. El-Ghenymy, R.M. Rodríguez, E. Brillas, N. Oturan, M.A. Oturan, Electro-Fenton degradation of the antibiotic sulfanilamide with Pt/carbon-felt and BDD/carbon-felt cells. Kinetics, reaction intermediates, and toxicity assessment, *Environ. Sci. Pollut. Res.* 21 (2014) 8368–8378.
 - [29] V. Poza-Nogueiras, E. Rosales, M. Pazos, M.Á. Sanromán, Current advances and trends in electro-Fenton process using heterogeneous catalysts – a review, *Chemosphere* 201 (2018) 399–416.
 - [30] S.O. Ganiyu, M. Zhou, C.A. Martínez-Huitle, Heterogeneous electro-Fenton and photoelectro-Fenton processes: a critical review of fundamental principles and application for water/wastewater treatment, *Appl. Catal. B* 235 (2018) 103–129.
 - [31] H.Y. Sheng, A.N. Janes, R.D. Ross, D. Kaiman, J.Z. Huang, B. Song, J.R. Schmidt, S. Jin, Stable and selective electrosynthesis of hydrogen peroxide and the electro-Fenton process on CoSe_2 polymorph catalysts, *Energy Environ. Sci.* 13 (2020) 4189–4203.
 - [32] L. Cui, X. Zhao, H. Xie, Z. Zhang, Overcoming the activity–stability trade-off in heterogeneous electro-Fenton catalysis: encapsulating carbon cloth-supported iron oxychloride within graphitic layers, *ACS Catal.* 12 (2022) 13334–13348.
 - [33] D.L. Guo, Y.B. Liu, H.D. Ji, C.C. Wang, B. Chen, C.S. Shen, F. Li, Y.X. Wang, P. Lu, W. Liu, Silicate-enhanced heterogeneous flow-through Electro-Fenton system using iron oxides under nanoconfinement, *Environ. Sci. Technol.* 55 (2021) 4045–4053.
 - [34] X. Qin, P.K. Cao, X. Quan, K. Zhao, S. Chen, H.T. Yu, Y. Su, Highly efficient hydroxyl radicals production boosted by the atomically dispersed Fe and Co sites for heterogeneous Electro-Fenton oxidation, *Environ. Sci. Technol.* 57 (2023) 2907–2917.
 - [35] K. Zhao, X. Quan, Y. Su, X. Qin, S. Chen, H.T. Yu, Enhanced chlorinated pollutant degradation by the synergistic effect between dechlorination and hydroxyl radical oxidation on a bimetallic single-atom catalyst, *Environ. Sci. Technol.* 55 (2021) 14194–14203.
 - [36] H. Wang, C. Tang, L. Wang, Z. Sun, X. Hu, MOF-derived Co/Fe@NPC-500 with large amounts of low-valent metals as an electro-Fenton cathode for efficient degradation of ceftazidime, *Appl. Catal. B Environ.* 333 (2023), 122755.
 - [37] Z. Wang, Q.-K. Li, C. Zhang, Z. Cheng, W. Chen, E.A. McHugh, R.A. Carter, B. I. Yakobson, J.M. Tour, Hydrogen peroxide generation with 100% Faradaic efficiency on metal-free carbon black, *ACS Catal.* 11 (2021) 2454–2459.
 - [38] C. Xia, Y. Xia, P. Zhu, L. Fan, H. Wang, Direct electrosynthesis of pure aqueous H_2O_2 solutions up to 20% by weight using a solid electrolyte, *Science* 366 (2019) 226–231.
 - [39] X.-j Yang, X.-m Xu, J. Xu, Y.-f Han, Iron oxychloride (FeOCl): an efficient Fenton-like catalyst for producing hydroxyl radicals in degradation of organic contaminants, *J. Am. Chem. Soc.* 135 (2013) 16058–16061.
 - [40] Y. Liu, X. Quan, X. Fan, H. Wang, S. Chen, High-yield electrosynthesis of hydrogen peroxide from oxygen reduction by hierarchically porous carbon, *Angew. Chem. Int. Ed.* 54 (2015) 6837–6841.
 - [41] H. Roth, Y. Gendel, P. Buzatu, O. David, M. Wessling, Tubular carbon nanotube-based gas diffusion electrode removes persistent organic pollutants by a cyclic adsorption – Electro-Fenton process, *J. Hazard. Mater.* 307 (2016) 1–6.
 - [42] E. Mousset, Z.T. Ko, M. Syafiq, Z. Wang, O. Lefebvre, Electrocatalytic activity enhancement of a graphene ink-coated carbon cloth cathode for oxidative treatment, *Electrochim. Acta* 222 (2016) 1628–1641.
 - [43] B.-Q. Li, C.-X. Zhao, J.-N. Liu, Q. Zhang, Electrosynthesis of hydrogen peroxide synergistically catalyzed by atomic Co- N_x -C sites and oxygen functional groups in noble-metal-free electrocatalysts, *Adv. Mater.* 31 (2019) 1808173.
 - [44] Y. Sun, S. Li, Z.P. Jovanov, D. Bernsmeier, H. Wang, B. Paul, X. Wang, S. Kühn, P. Strasser, Structure, activity, and faradaic efficiency of nitrogen-doped porous carbon catalysts for direct electrochemical hydrogen peroxide production, *ChemSusChem* 11 (2018) 3388–3395.
 - [45] S. Chen, Z. Chen, S. Siahrostami, D. Higgins, D. Nordlund, D. Sokaras, T.R. Kim, Y. Liu, X. Yan, E. Nilsson, R. Sinclair, J.K. Nørskov, T.F. Jaramillo, Z. Bao, Designing boron nitride islands in carbon materials for efficient electrochemical synthesis of hydrogen peroxide, *J. Am. Chem. Soc.* 140 (2018) 7851–7859.
 - [46] X. Qin, K. Zhao, X. Quan, P. Cao, S. Chen, H. Yu, Highly efficient metal-free electro-Fenton degradation of organic contaminants on a bifunctional catalyst, *J. Hazard. Mater.* 416 (2021), 125859.
 - [47] J. Xu, X. Zheng, Z. Feng, Z. Lu, Z. Zhang, W. Huang, Y. Li, D. Vuckovic, Y. Li, S. Dai, G. Chen, K. Wang, H. Wang, J.K. Chen, W. Mitch, Y. Cui, Organic wastewater treatment by a single-atom catalyst and electrolytically produced H_2O_2 , *Nat. Sustain.* 4 (2021) 233–241.
 - [48] O. Scialdone, A. Galia, C. Gattuso, S. Sabatino, B. Schiavo, Effect of air pressure on the electro-generation of H_2O_2 and the abatement of organic pollutants in water by electro-Fenton process, *Electrochim. Acta* 182 (2015) 775–780.
 - [49] Y. Zheng, J. He, S. Qiu, D. Yu, Y. Zhu, H. Pang, J. Zhang, Boosting hydrogen peroxide accumulation by a novel air-breathing gas diffusion electrode in electro-Fenton system, *Appl. Catal. B* 316 (2022), 121617.
 - [50] C. Tang, H.-F. Wang, Q. Zhang, Multiscale principles to boost reactivity in gas-involving energy electrocatalysis, *Acc. Chem. Res.* 51 (2018) 881–889.
 - [51] Y. Zhang, G. Daniel, S. Lanzalaco, A.A. Isse, A. Faccin, A. Wang, E. Brillas, C. Durante, I. Sirés, H_2O_2 production at gas-diffusion cathodes made from agarose-derived carbons with different textural properties for acetobutolol degradation in chloride media, *J. Hazard. Mater.* 423 (2022), 127005.
 - [52] W. Zhang, J.W. Choi, S. Kim, T.T. Le, S. Nandy, C.-K. Hwang, S.Y. Paek, A. Byeon, K.H. Chae, S.Y. Lee, S.H. Kim, H. Song, J. Kim, J. Oh, J.W. Lee, S.S. Han, J.M. Kim, Penta nitrogen coordinated cobalt single atom catalysts with oxygenated carbon black for electrochemical H_2O_2 production, *Appl. Catal. B Environ.* 331 (2023), 122712.
 - [53] N. Le-Minh, S.J. Khan, J.E. Drewes, R.M. Stuetz, Fate of antibiotics during municipal water recycling treatment processes, *Water Res.* 44 (2010) 4295–4323.
 - [54] A. Puga, M.M. Moreira, S.A. Figueiredo, C. Delerue-Matos, M. Pazos, E. Rosales, M.Á. Sanromán, Electro-Fenton degradation of a ternary pharmaceutical mixture and its application in the regeneration of spent biochar, *J. Electroanal. Chem.* 886 (2021), 115135.
 - [55] Y. Yao, L. Lai, Z. Yu, Y. Pan, Y. Yu, V. Lo, A. Roy, B. Chivers, X. Zhong, L. Wei, Y. Chen, Carbon/iron by-product from catalytic methane decomposition as recyclable Fenton catalyst for pollutant degradation, *J. Hazard. Mater.* 437 (2022), 129328.
 - [56] H. Lin, N. Oturan, J. Wu, M.A. Oturan, H. Zhang, The application of electro-fenton process for the treatment of artificial sweeteners, in: M. Zhou, M.A. Oturan, I. Sirés (Eds.), *Electro-Fenton Process: New Trends and Scale-Up*, Springer Singapore, Singapore, 2018, pp. 379–398.
 - [57] X. Sheng, J. Wang, Q. Cui, W. Zhang, X. Zhu, A feasible biochar derived from biogas residue and its application in the efficient adsorption of tetracycline from an aqueous solution, *Environ. Res.* 207 (2022), 112175.
 - [58] M. Kończak, A. Siatecka, M.A. Nazarkovsky, B. Czech, P. Oleszczuk, Sewage sludge and solid residues from biogas production derived biochar as an effective bio-waste adsorbent of fulvic acids from water or wastewater, *Chemosphere* 278 (2021), 130447.
 - [59] X. Zhang, Y. Li, M. Wu, Y. Pang, Z. Hao, M. Hu, R. Qiu, Z. Chen, Enhanced adsorption of tetracycline by an iron and manganese oxides loaded biochar: kinetics, mechanism and column adsorption, *Bioresour. Technol.* 320 (2021), 124264.
 - [60] R. Antón-Herrero, C. García-Delgado, M. Alonso-Izquierdo, G. García-Rodríguez, J. Cuevas, E. Eymar, Comparative adsorption of tetracyclines on biochars and stevenson: looking for the most effective adsorbent, *Appl. Clay Sci.* 160 (2018) 162–172.
 - [61] A.L.P.F. Caroni, C.R.M. de Lima, M.R. Pereira, J.L.C. Fonseca, Tetracycline adsorption on chitosan: a mechanistic description based on mass uptake and zeta potential measurements, *Colloids Surf. B Biointerfaces* 100 (2012) 222–228.
 - [62] L. Du, S. Ahmad, L. Liu, L. Wang, J. Tang, A review of antibiotics and antibiotic resistance genes (ARGs) adsorption by biochar and modified biochar in water, *Sci. Total Environ.* 858 (2023), 159815.
 - [63] H.M. Jang, S. Yoo, Y.-K. Choi, S. Park, E. Kan, Adsorption isotherm, kinetic modeling and mechanism of tetracycline on Pinus taeda-derived activated biochar, *Bioresour. Technol.* 259 (2018) 24–31.
 - [64] Y. Zhou, X. Liu, Y. Xiang, P. Wang, J. Zhang, F. Zhang, J. Wei, L. Luo, M. Lei, L. Tang, Modification of biochar derived from sawdust and its application in removal of tetracycline and copper from aqueous solution: adsorption mechanism and modelling, *Bioresour. Technol.* 245 (2017) 266–273.
 - [65] L. Wang, D. Zhu, L. Duan, W. Chen, Adsorption of single-ringed N- and S-heterocyclic aromatics on carbon nanotubes, *Carbon* 48 (2010) 3906–3915.
 - [66] Y. Gao, Y. Li, L. Zhang, H. Huang, J. Hu, S.M. Shah, X. Su, Adsorption and removal of tetracycline antibiotics from aqueous solution by graphene oxide, *J. Colloid Interface Sci.* 368 (2012) 540–546.
 - [67] Z. Li, L. Schulz, C. Ackley, N. Fenske, Adsorption of tetracycline on kaolinite with pH-dependent surface charges, *J. Colloid Interface Sci.* 351 (2010) 254–260.

- [68] M.E. Parolo, M.C. Savini, J.M. Vallés, M.T. Baschini, M.J. Avena, Tetracycline adsorption on montmorillonite: pH and ionic strength effects, *Appl. Clay Sci.* 40 (2008) 179–186.
- [69] P. Cao, X. Quan, X. Nie, K. Zhao, Y. Liu, S. Chen, H. Yu, J.G. Chen, Metal single-site catalyst design for electrocatalytic production of hydrogen peroxide at industrial-relevant currents, *Nat. Commun.* 14 (2023) 172.
- [70] Q. Zhang, M. Zhou, G. Ren, Y. Li, Y. Li, X. Du, Highly efficient electrosynthesis of hydrogen peroxide on a superhydrophobic three-phase interface by natural air diffusion, *Nat. Commun.* 11 (2020) 1731.
- [71] Z. Lu, G. Chen, S. Siahrostami, Z. Chen, K. Liu, J. Xie, L. Liao, T. Wu, D. Lin, Y. Liu, T.F. Jaramillo, J.K. Nørskov, Y. Cui, High-efficiency oxygen reduction to hydrogen peroxide catalysed by oxidized carbon materials, *Nat. Catal.* 1 (2018) 156–162.
- [72] H.W. Kim, M.B. Ross, N. Kornienko, L. Zhang, J. Guo, P. Yang, B.D. McCloskey, Efficient hydrogen peroxide generation using reduced graphene oxide-based oxygen reduction electrocatalysts, *Nat. Catal.* (2018).
- [73] X. Zhang, X. Zhao, P. Zhu, Z. Adler, Z.-Y. Wu, Y. Liu, H. Wang, Electrochemical oxygen reduction to hydrogen peroxide at practical rates in strong acidic media, *Nat. Commun.* 13 (2022) 2880.
- [74] S.B. Hammouda, F. Fourcade, A. Assadi, I. Soutrel, N. adhoum, A. Amrane, L. Monser, Effective heterogeneous electro-Fenton process for the degradation of a malodorous compound, indole, using iron loaded alginate beads as a reusable catalyst, *Appl. Catal. B* 182 (2016) 47–58.
- [75] T. Luo, H. Feng, L. Tang, Y. Lu, W. Tang, S. Chen, J. Yu, Q. Xie, X. Ouyang, Z. Chen, Efficient degradation of tetracycline by heterogeneous electro-Fenton process using Cu-doped Fe@Fe₂O₃: mechanism and degradation pathway, *Chem. Eng. J.* 382 (2020), 122970.
- [76] F. Xiao, Z. Wang, J. Fan, T. Majima, H. Zhao, G. Zhao, Selective electrocatalytic reduction of oxygen to hydroxyl radicals via 3-electron pathway with FeCo alloy encapsulated carbon aerogel for fast and complete removing pollutants, *Angew. Chem. Int. Ed.* 60 (2021) 10375–10383.
- [77] X. Cheng, L. Liang, J. Ye, N. Li, B. Yan, G. Chen, Influence and mechanism of water matrices on H₂O₂-based Fenton-like oxidation processes: a review, *Sci. Total Environ.* 888 (2023), 164086.